Hindawi
International Journal of Antennas and Propagation
Volume 2022, Article ID 3887314, 12 pages
https://doi.org/10.1155/2022/3887314

Research Article

A Comparison between Multiple-Input Multiple-Output and Multiple-Input Single-Output Radar Configurations for Through-the-Wall Imaging Applications

Stefano Pisa, Renato Cicchetti, Emanuele Piuzzi, and Orlandino Testa

Department of Information Engineering, Electronics and Telecommunications, Sapienza University of Rome, Rome 00184, Italy

Correspondence should be addressed to Stefano Pisa; stefano.pisa@uniroma1.it

Received 8 February 2022; Revised 13 April 2022; Accepted 21 April 2022; Published 31 May 2022

Academic Editor: Mohammad Alibakhshikenari

The performances of a multiple-input multiple-output (MIMO) radar, employing 16 equivalent antennas, and multiple-input single-output (MISO) radar, employing 10 antennas, for through-the-wall imaging applications are analyzed. In particular, imaging algorithms based on the Fourier transform (FT) and the multiple signal classification (MUSIC) available in the literature are compared with the FT-MUSIC hybrid algorithm recently developed by the authors. Three different investigations have been performed. The first, performed analytically, refers to a scenario in which a point scatterer is placed in free space, and the second, addressed numerically using the CST full-wave software, refers to a scenario in which two targets are present, while the last was executed in a real scenario where a metal panel is placed behind a tuff wall. All the algorithms and radar configurations were found to be suitable for accurately reconstructing the position of the investigated target. In particular, applying the FT technique, the MISO configuration has a lower cross-range half-power beamwidths (HPBW) than the MIMO one, while the range HPBW is the same for the two radar configurations. Despite the different number of elements present in the two radar configurations, similar range and cross-range HPBW are obtained for both configurations when MUSIC and FT-MUSIC techniques are employed. The field of view for FT and FT-MUSIC is about 45°, while it is less than 15° for the MUSIC algorithm. The HPBWs obtained with the experimental setup are very close to those obtained in the analytical study. Finally, the proposed experimental MISO radar acquires the data in half the time required by the MIMO one. The numerical results, confirmed by the experimental measurements, seem to indicate in the FT-MUSIC technique the one that provides the best performance for the considered radar configurations.

1. Introduction

Short-range radars are used in automotive applications for automatic cruise control, collision mitigation braking, and blind spot detection [1]. These radars can also be used for through-the-wall imaging applications and, therefore, can be useful for police, firefighters, and defense forces to detect, identify, and track individuals inside buildings or under rubbles [2]. Furthermore, they can also be used to monitor the elderly activity into their home [3]. Typically, these systems are based on frequency modulated continuous wave (FMCW) [4, 5], ultrawide band (UWB) [6, 7], or step frequency (SF) [8, 9] modulations.

The stepped frequency radar (SFR) transmits a series of discrete frequencies in a stepwise manner covering the radar bandwidth. SFRs have been used to detect cardiorespiratory signals from a human subject positioned behind obstacles under controlled laboratory conditions [10].

However, these SFRs use a single-input single-output (SISO) channel, and therefore, only range movements of humans can be measured. SISO radars have been also realized by using FMCW [11] or UWB [12] architectures. The radar system with multiple receiving channels, termed as multiple-input single-output (MISO), is then used to achieve target localization. Liu et al. [13] demonstrated that the MISO radar systems have the ability to measure the breathing activity and obtain the angle of arrival (AOA) of multiple human targets. Akiyama et al. [14] used a system with one transmitting and four receiving antennas and extracted respiratory activity by improving the signal-to-noise ratio (SNR) using signal

correlation processing. Multiple-input multiple-output (MIMO) radar utilizes an array with M transmitting and N receiving elements so obtaining an aperture with $M \times N$ virtual transceivers. MIMO radar combines the high-range resolution property of the UWB signal with the spatial resolution property due to the multiple antenna elements, so it has the ability to perform two-dimensional high-resolution imaging. With a MIMO radar system, a sequence of images can be achieved, and at the same time, the changes in the scenario over time followed. Salmi and Molisch [15] realized a MIMO radar able to localize a test subject and track his breathing, while Liang et al. [16] proposed a novel method to detect and localize multiple stationary humans by suppressing the environmental clutter. Quinquis et al. [17] applied subspace Eigen analysis-based methods to the MIMO radar imaging of scale reduced aircraft models in order to evaluate their scattering center locations and to identify the target, while in [18] a new hybrid technique based on the MUSIC algorithm was proposed for through the wall radar imaging of multiple scatterers. To suppress the artefacts appearing in the reconstructed image and to reduce the computing complexity, Hu et al. applied the cross-correlation-based time domain back projection (CC-TDBP) algorithm [19]. In [9], a MIMO system with 4 transmitting and 4 receiving antennas was proposed. Delay and Sum (DAS) [20, 21], Fourier transform (FT) [4, 22], multiple signal classification (MUSIC) [17, 18], DAS-MUSIC [18], and a new FT-MUSIC algorithm were used for the scenario reconstruction. The elaboration time of the various algorithms was investigated evidencing values between few seconds for the FT algorithm up to hundreds of seconds for the DAS-MUSIC one [9]. Another factor influencing the scenario scan rate is the time necessary to the system to acquire the data used for the image reconstruction. For the MIMO configuration presented in [9], this time was about 20 s. To increase the scan rate, a multiple-input single-output (MISO) configuration has been proposed utilizing a reduced number of equivalent antennas [23].

Many MISO and MIMO systems proposed in the literature use only one transmitting and one receiving antenna, which are then moved to various positions to achieve an equivalent array allowing to find the cross-range location of the target. No comparison is reported in terms of resolution, field of view, and elaboration/acquisition times between a MISO and a MIMO system having the same geometry. To this end, in this paper, the half power beam width in range and cross-range, the angular extension, and the computation times of MIMO and MISO radar configurations are compared by using an experimental setup based on an array of Vivaldi antennas having the same vertical and horizontal extension for the two considered radar configurations. FT, MUSIC, and FT-MUSIC algorithms are used for the image reconstruction. In particular, MIMO and MISO radar configurations and reconstruction techniques are numerically compared considering a canonical scenario consisting of a point scatterer, and an environment where two targets are present. Finally, a real scenario, in which a metal panel is placed behind a tuff wall, has been considered to validate the algorithms.

2. Materials and Methods

2.1. Experimental Setup. The schematics of the MIMO and MISO radar systems are reported in Figure 1(a) and 1(b), respectively. Both systems utilize the Agilent M5230 A vector network analyzer (VNA), with a 110 dB dynamic range, and 0 dBm output power.

The VNA measures the transmission scattering parameter (S_{21}) between the transmitting and the receiving sections for N_a antenna positions and $N_f = 501$ frequency points between 1 GHz and 3 GHz. For measurements in the presence of the wall, a 15 dB power amplifier (HP 8349A) (not shown in the figure) is added in the transmission channel. All driving signals are provided by the National Instruments DAQ board NI USB-6251, which is controlled by a program written in the LabVIEW environment. In turn, the scattering parameters measured by the VNA are acquired through a GPIB interface. The complex scattering parameters are saved in a $(N_a \times N_f)$ matrix. Finally, the imaging algorithms implemented in MATLAB are applied to the collected data stored in the aforementioned matrix. For the MIMO configuration shown in Figure 1(a), a couple of SP4T switches (Pasternak PE71S6088) select sequentially a transmitting (TX) Vivaldi antenna and a receiving (RX) Vivaldi antenna [9, 24]. The spatial positioning of TX and RX antennas is chosen as indicated in Figure 2(a).

In this way, a series of $N_a = 16$ equidistant equivalent antennas separated by a quarter of free space wavelength at 2 GHz is achieved. Following the spatial positioning indicated in Figure 2(a), eight antennas are housed in a wooden box (see Figure 2(b)). Concerning the MISO system, Port 1 of the VNA is connected to a transmitting Vivaldi antenna, while Port 2 is connected to a system of switches able of selecting $N_a = 10$ receiving Vivaldi antennas. The antennas are selected via 3 electrically controlled switches. The first is the Analog Devices HMC344ALP3E, which is driven by two control pins with negative signals. Two of the four RF outputs of the switch are connected to the input of two electromechanical switches (Pasternak PE71S6088). These switches are driven with TTL logic, and five of the six output channels are connected to the 10 receiving antennas (see schematic of the MISO radar shown in Figure 1(b)). The spatial positioning of the antennas is chosen as indicated in Figure 3(a).

In this way, a series of 10 equidistant equivalent antennas separated by a quarter of free-space wavelength at the central frequency of 2 GHz is realized. Following the spatial positioning indicated in Figure 3(a), the antennas are housed in the same wooden box used for the MIMO system (see Figure 3(b)). Before taking the measurements, both systems are calibrated between the port of the transmitting antenna and the port of one receiving antenna. The measurement error due to the propagation delay of the signal introduced by the Vivaldi antennas has been estimated and corrected by means of the experimental measurement procedure described in [9]. Collecting the experimental data in accordance with the procedure indicated in [9], a value of about 2.32 ns for the delay introduced by the antenna system was obtained. The adoption of the HP8349A amplifier in the

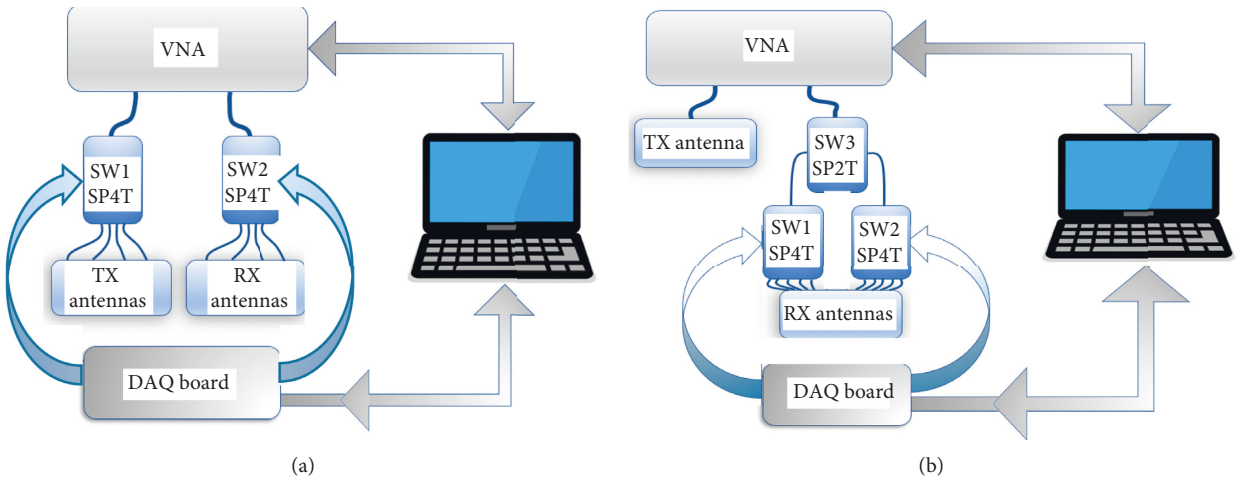

Figure 1: Schematic of the realized MIMO (a) and MISO (b) radar.

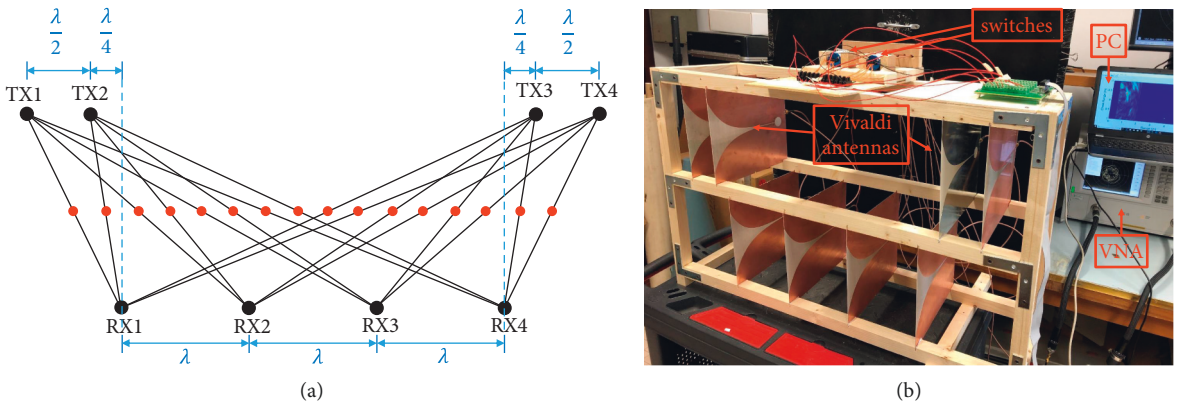

Figure 2: Antenna topology of a MIMO radar system (a) and hardware realization of the antenna system (b).

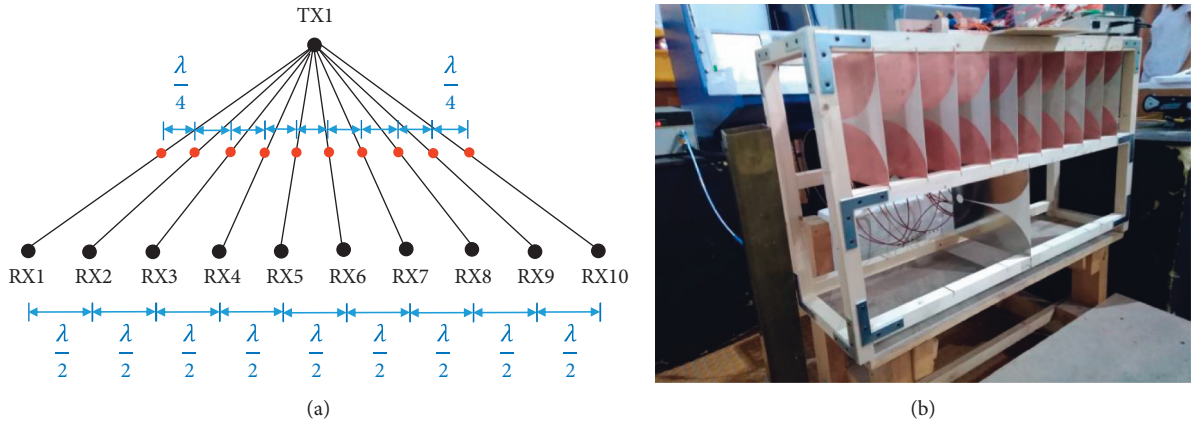

Figure 3: Antenna topology of a MISO radar system (a) and hardware realization of the antenna system (b).

transmission channel produces a further delay of 5 ns, which has been evaluated by the phase slope of the S_{21} scattering parameter of the amplifier.

2.2. Reconstruction Algorithms. The considered radar system is composed of N_a (even) rice-transmitting antennas located at position (x_p, y_p) along the x–axis with a uniform spacing d_a [see Figure 4(a)].

The reflection coefficients of each of the N_a antennas are evaluated at uniformly spaced N_f frequency values f_q between $f_{\min}$ and $f_{\max}$ (frequency bandwidth $B = f_{\max} - f_{\min}$) and recorded in a Γ matrix, having Γ_{pq} as a

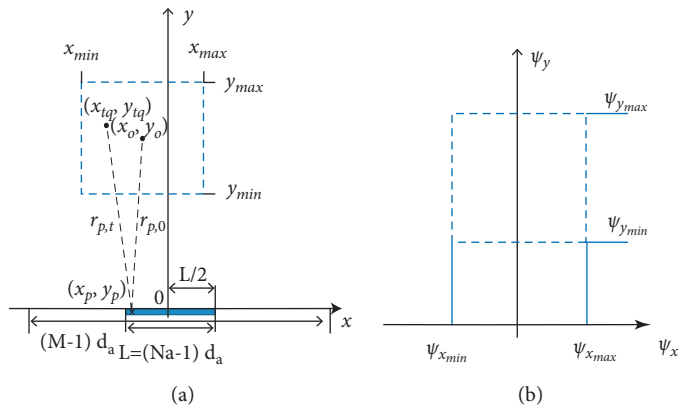

FIGURE 4: Geometry of the scenario: x-y plane (a) and $\psi_x - \psi_y$ plane (b).

generic element. The parameters x_p and f_q above indicated are defined as follows:

$$x_p = \left(p + \frac{1}{2}\right) d_a, \quad p = -\frac{N_a}{2}, \ldots, \frac{N_a}{2} - 1, \tag{1}$$

$$f_q = f_{\min} + \frac{B}{N_f - 1} q, \quad q = 0, \ldots, N_f - 1. \tag{2}$$

Starting from (1) and (2), the following wavenumbers are defined and sampled at M and N points in cross-range and range, respectively:

$$\begin{aligned} \psi_{x_u} &= u \frac{2\pi}{M d_a}, \quad u = -\frac{M}{2}, \ldots, \frac{M}{2} - 1, \\ \psi_{y_v} &= \psi_{y_{\min}} + v \frac{\psi_{y_{\max}} - \psi_{y_{\min}}}{N - 1}, \quad v = 0, .., N - 1, \end{aligned} \tag{3}$$

where

$$\begin{aligned} \psi_{y_{\min}} &= \frac{4\pi f_{\min}}{c}, \\ \psi_{y_{\max}} &= \sqrt{\left(\frac{4\pi f_{\max}}{c}\right)^2 - \left(\frac{\pi}{d_a}\right)^2}. \end{aligned} \tag{4}$$

Then, the region of interest (ROI) [dashed blue box in Figure 4(a)] is subdivided into $N_x \times N_y$ square pixels having coordinates

$$\begin{aligned} x_s &= x_{\min} + \frac{x_{\max} - x_{\min}}{N_x - 1} s \quad s = 0, \ldots, N_x - 1, \\ y_r &= y_{\min} + \frac{y_{\max} - y_{\min}}{N_y - 1} r \quad r = 0, \ldots, N_y - 1. \end{aligned} \tag{5}$$

Since the reconstruction techniques considered in this paper have been described in [9], for the reader convenience, only the main formulation is reported. The Fourier transform (FT) technique is based on the cross-range FT of the reflection coefficients Γ_{pq}. This is achieved applying the FFT to all columns of Γ_{pq} coefficients with a M (even) sampling, obtaining

$$\tilde{\Gamma}_{uq} = \tilde{\Gamma}(\omega, \psi_x)\big|_{\substack{\omega = \omega_q \\ \psi_x = \psi_{x_u}}} = d_a e^{j\psi_{x_u}(L/2 + x_0)} \sum_{p=0}^{N_a - 1} \Gamma_{pq} e^{-j2\pi u\, p/M}. \tag{6}$$

To express (6) in a regular rectangular grid (u, v) associated with the variables ψ_x, ψ_y [see Figure 1(b)], a 3rd-order polynomial interpolation is used, thus obtaining the following:

$$\begin{aligned} \tilde{\Gamma}_{uv} &= \tilde{\Gamma}(\omega, \psi_x) e^{j\psi_{y_v}(y_0 - y_p)}\big|_{\omega = \frac{c}{2}\sqrt{\psi_{x_u}^2 + \psi_{y_v}^2}} \\ &\quad \psi_x = \psi_{x_u} \end{aligned} \tag{7}$$

Finally, the FT intensity function in the ROI is evaluated as follows:

$$I_{\mathrm{FT}sr} = \left| \sum_{u=-M/2}^{M/2-1} \sum_{v=0}^{N-1} \tilde{\Gamma}_{uv} e^{j\psi_{x_u}(x_s - x_0)} e^{j\psi_{y_v}(y_r - y_0)} \right|. \tag{8}$$

The second considered reconstruction algorithm is the MUSIC one. As first step, the algorithm employs a partial compensation of the rapid phase variation of Γ_{pq} coefficients performed as follows:

$$\bar{\Gamma}_{pq} = \Gamma_{pq} \exp\left\{\frac{j4\pi f_q r_{p,o}}{c}\right\}, \tag{9}$$

where $r_{p,o}$ identifies the distance between the p-th array antenna and the ROI center [see Figure 4(a)]. Then, the coefficients $\bar{\Gamma}_{pq}$ are linked to the transverse ψ_x and longitudinal ψ_y wavenumbers, achieving

$$\begin{aligned} \bar{\bar{\Gamma}}_{pq} &= \bar{\bar{\Gamma}}(\psi_x, \psi_y)\Big|_{\psi_x = -2\frac{\omega_q}{c}\frac{x_p - x_0}{r_{p,o}}} \\ &\quad \psi_y = -2\frac{\omega_q}{c}\frac{y_p - y_0}{r_{p,o}} \end{aligned} \tag{10}$$

Subsequently, a 3rd-order polynomial interpolation is performed to express (10) by means of the (u, v) indexes obtaining

$$\bar{\Gamma}_{uv}' = \bar{\Gamma}\left(\psi_{x_{u'}}, \psi_{y_v}\right), \quad u = -\frac{M}{2}, \ldots, \frac{M}{2} - 1, v = 0, \ldots, N-1. \tag{11}$$

The MUSIC algorithm is derived introducing the flattener operator

$$\underline{\boldsymbol{\varrho}} = \mathbf{F}_l\left(\underline{\boldsymbol{\chi}}\right) = \left[\chi_{11} \cdots \chi_{M1} \chi_{12} \cdots \chi_{M2} \cdots \chi_{MN}\right]^T, \tag{12}$$

where $\underline{\boldsymbol{\chi}}$ is a matrix of size $M \times N$, and $\underline{\boldsymbol{\varrho}}$ is a vector having $M \cdot N$ elements, while $(\cdot)^T$ denotes the transpose operator. The discrete form of the covariance operator can be written in the following compact form [18]:

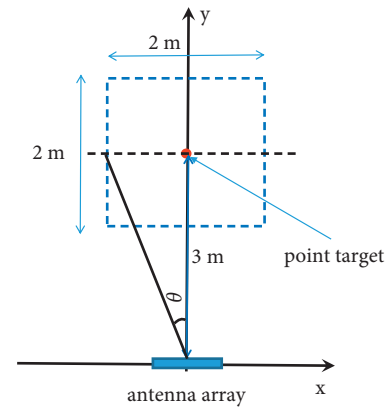

Figure 5: Geometry of the simulated scenario with antenna array and a single point scatterer in free space.

$$\underline{\mathbf{R}} = \frac{1}{2N_S} \sum_{u=-M/2}^{M/2-K+1} \sum_{v=1}^{N-L+1} \left[\mathbf{F}_l\left(\underline{\chi}_{uv}\right) \cdot \mathbf{F}_l\left(\underline{\chi}_{uv}\right)^H + \underline{\mathbf{J}} \cdot \mathbf{F}_l\left(\underline{\chi}_{uv}\right)^* \cdot \mathbf{F}_l\left(\underline{\chi}_{uv}\right)^T \cdot \underline{\mathbf{J}}\right], \tag{13}$$

where $\underline{\chi}_{uv}$ are $K \times L$ submatrices extracted from the matrix $\bar{\bar{\Gamma}}_{uv}'$, starting from u and v indexes, which address the first element of the submatrix; $\underline{\mathbf{J}}$ is a square $KL \times KL$ matrix having a unitary value on the secondary diagonal; $(\cdot)^*$ denotes the complex conjugate operator; $(\cdot)^H$ denotes the Hermitian transpose operator; and $N_S = (M - K + 1)(N - L + 1)$. Consequently, the covariance matrix $\underline{\mathbf{R}}$ has size $KL \times KL$. According to the theory presented in [18], $\underline{\mathbf{R}}$ should have a number N_H of the highest eigenvalues equal to the number of targets N_T. Using the N_H normalized eigenvectors $\mathbf{w}_u$ of $\underline{\mathbf{R}}$ linked to the N_H highest eigenvalues, the following operator is defined:

$$\underline{\mathbf{Q}} = \underline{\mathbf{1}} - \sum_{u=1}^{N_H} \mathbf{w}_u \cdot \mathbf{w}_u^H, \tag{14}$$

where $\underline{\mathbf{1}}$ is the unitary dyad. Finally, the intensity function $I_{\mathrm{MUSIC}_{u,v}}$ is obtained using the following expression:

$$I_{\mathrm{MUSIC}_{u,v}} = \frac{1}{\mathbf{a}\left(x_u, y_v\right)^H \cdot \underline{\mathbf{Q}} \cdot \mathbf{a}\left(x_u, y_v\right)}, \tag{15}$$

where the vector $\mathbf{a}(x, y)$ is given by

$$\mathbf{a}(x, y) = \frac{1}{\sqrt{KL}} \left[e^{-j\psi_{x_{-M/2}}(x - x_0) - j\psi_{y_0}(y - y_0)} \cdots e^{-j\psi_{x_{-M/2+K-1}}(x - x_0) - j\psi_{y_0}(y - y_0)} e^{-j\psi_{x_{-M/2}}(x - x_0) - j\psi_{y_1}(y - y_0)} \cdots \right.$$
$$\left. e^{-j\psi_{x_{-M/2+K-1}}(x - x_0) - j\psi_{y_1}(y - y_0)} \cdots e^{-j\psi_{x_{-M/2+K-1}}(x - x_0) - j\psi_{y_{L-1}}(y - y_0)}\right]^T. \tag{16}$$

The third considered algorithm is the FT-MUSIC one. This algorithm is derived by applying (13) and (14) to the $\bar{\bar{\Gamma}}$ matrix in (7) instead of $\bar{\bar{\Gamma}}'$ in (11). The intensity function $I_{FTMUSIC_{u,v}}$ is obtained using the following expression:

$$I_{\mathrm{FTMUSIC}_{u,v}} = \frac{1}{\mathbf{a}\left(x_u, y_v\right)^H \cdot \underline{\mathbf{Q}} \cdot \mathbf{a}\left(x_u, y_v\right)}, \tag{17}$$

where the vector $\mathbf{a}(x, y)$ is given by (16).

3. Results and Discussion

The previously described algorithms were used starting from analytical data concerning the simulated scattered field from a point scatterer and from data collected by measurements carried out considering a metallic panel, placed beyond a tuff wall, with the two radar configurations described in the experimental setup section.

Case 1. Point scatterer

For a point-like target, the reflection coefficient Γ_{pq} takes the following form:

$$\Gamma_{pq} \approx \sigma_q \exp\left\{-j4\pi f_q\left(\frac{r_{p,t}}{c}\right)\right\} + n_{pq}, \tag{18}$$

where n_{pq} is a white zero mean Gaussian noise with σ^2 variance, and σ_q is a coefficient linked to the radar cross-section of the target and to the electrical path of the RF

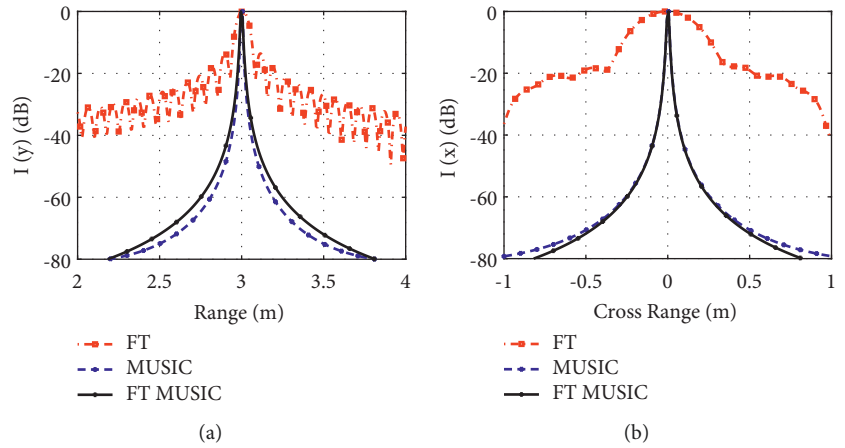

Figure 6: Comparison between the three considered techniques. Image cuts along the range (a) and cross-range (b) directions with the MIMO radar configuration.

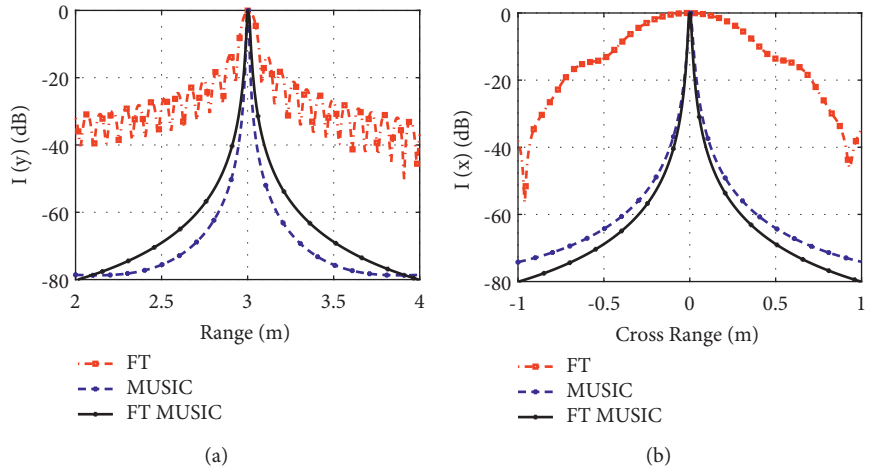

Figure 7: Comparison between the three considered techniques. Image cuts along the range (a) and cross-range (b) directions with the MISO radar configuration.

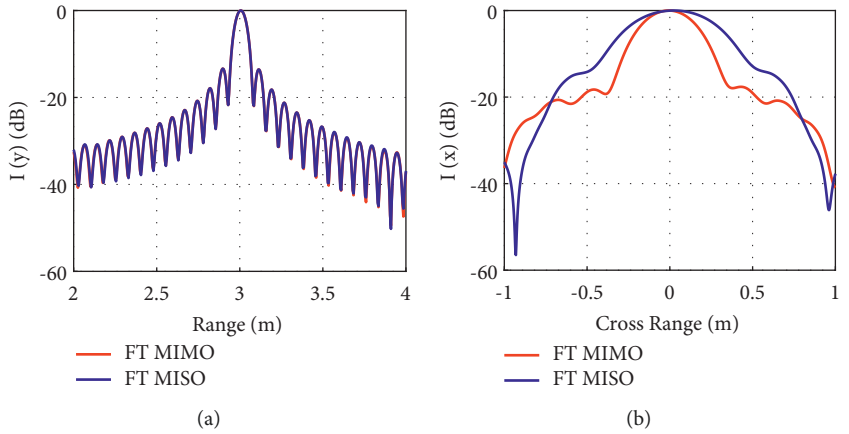

Figure 8: Comparison between the MIMO and MISO radar configurations. Image cuts along range (a) and cross-range (b) directions obtained with the FT technique.

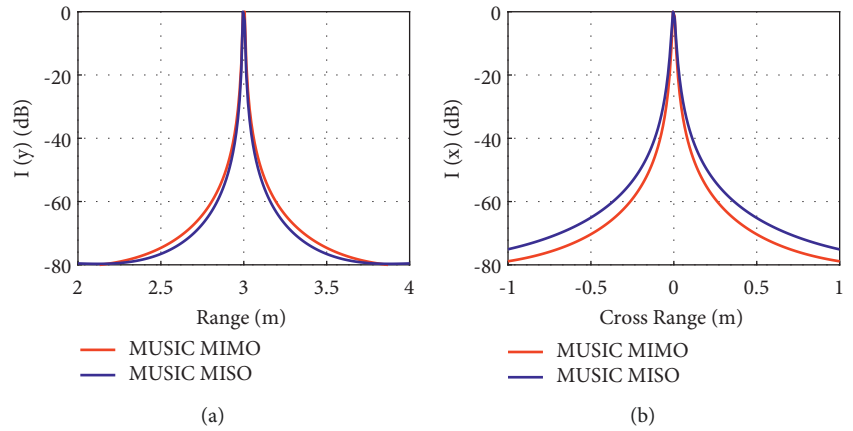

Figure 9: Comparison between the MIMO and MISO radar configurations. Image cuts along range (a) and cross-range (b) directions obtained with the MUSIC technique.

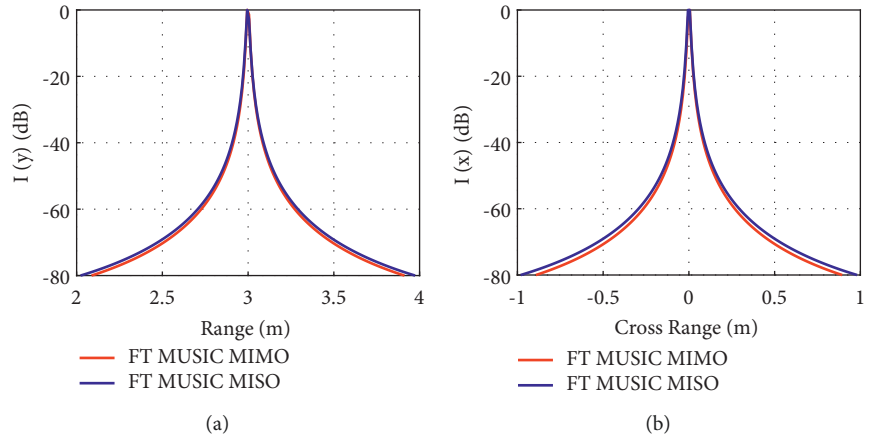

Figure 10: Comparison between the MIMO and MISO radar configurations. Image cuts along range (a) and cross-range (b) directions obtained with the FT-MUSIC technique.

signal, while $r_{p,t}$ is the distance between the antenna element located at (x_p, y_p) and the target located at (x_{t_q}, y_{t_q}) [see Figure 4(a)]. The investigated ROI consists of a $2\,m \times 2$ m square region subdivided into square cells with 1-cm side. (18) has been used to evaluate the scattering parameters at 501 frequency points between 1 and 3 GHz (frequency band $B = 2$ GHz and frequency step $\Delta f = 4$ MHz). A Gaussian noise with variance equal to $\sigma^2 = 0.1$ has been added to all the scattering parameters to take into account the environmental noise. This canonical scenario has been analyzed by considering two antenna arrays having the same geometry as the MIMO and MISO radar previously described. For the considered scenario, the radar theoretical resolution in range is $\delta r = c/2B = 7.5$ cm; the angular resolution is $\delta\theta = \lambda/2 \bullet d_a \bullet (N_a - 1) = 0.13$ rad (7.6°) and 0.22 rad (12.7°) for the MIMO and MISO configurations, respectively; and the unambiguous range is $R_{\max} = c/2\delta f = 37.5$ m. In particular, a point scatterer placed 3 m far from the antenna plane and centered with respect to the antenna array [see Figure 5] has been considered.

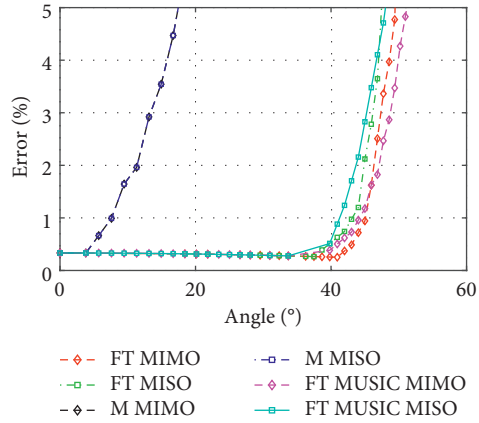

Figure 11: Estimate of the error on the target position versus the angle for the two considered radar configurations and for the three adopted reconstruction techniques.

Figures 6 and 7 show the results of the simulations performed by using the three considered techniques with the MIMO and MISO radar configurations, respectively. In

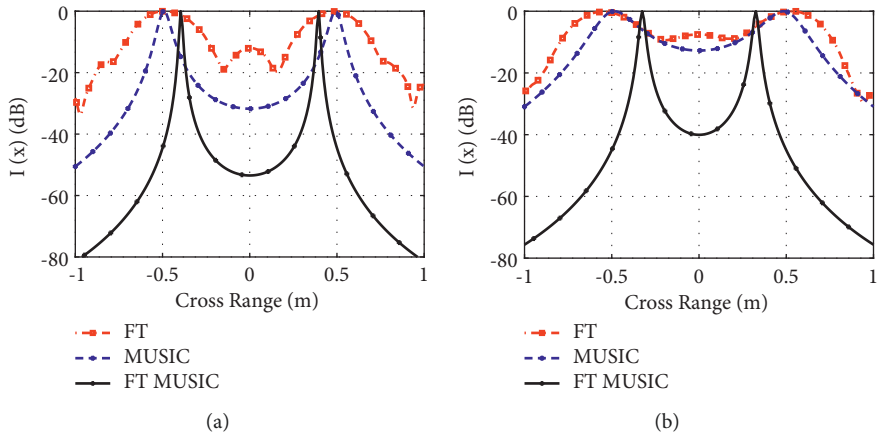

Figure 12: Comparison between the three considered techniques for a scenario with two targets. Image cuts along the cross-range directions for the MIMO (a) and MISO (b) radar configurations.

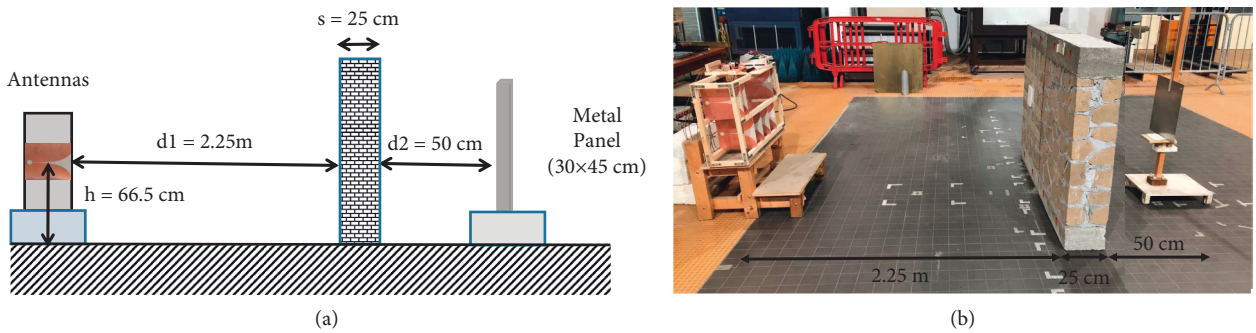

Figure 13: Schematic of the experimental investigated scenario (a) and photo of the radar configuration (b).

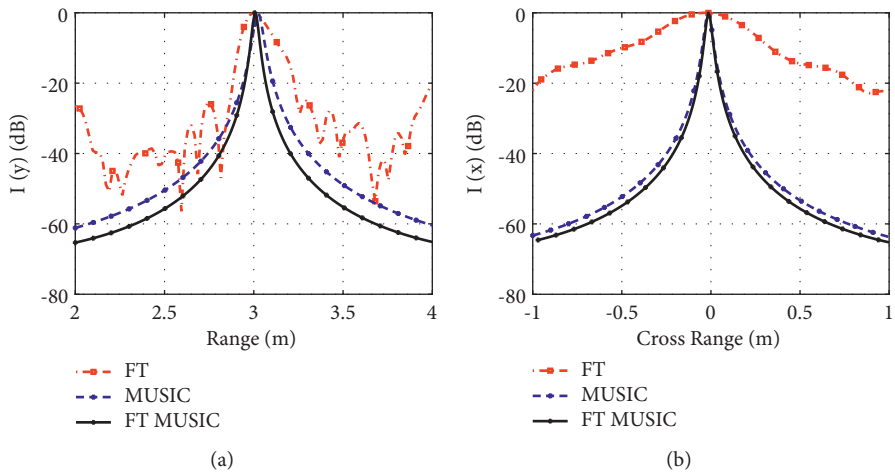

Figure 14: Image cuts along the range (a) and cross-range (b) directions with the MIMO radar configuration. A comparison between the three considered techniques is reported in the figure.

these figures, the normalized intensity function for the cuts along the range (a) and cross-range (b) directions performed on the image reconstructions based on the considered techniques have been reported. The figures show that both radar configurations and the three considered reconstruction techniques are able to correctly localize the target position. Moreover, MUSIC and FT-MUSIC algorithms present a similar behavior and a better resolution with respect to FT in particular along the cross-range direction.

Figures 8–10 show a direct comparison between the MIMO and MISO results for the FT (Figure 8), MUSIC (Figure 9), and FT-MUSIC (Figure 10) algorithms.

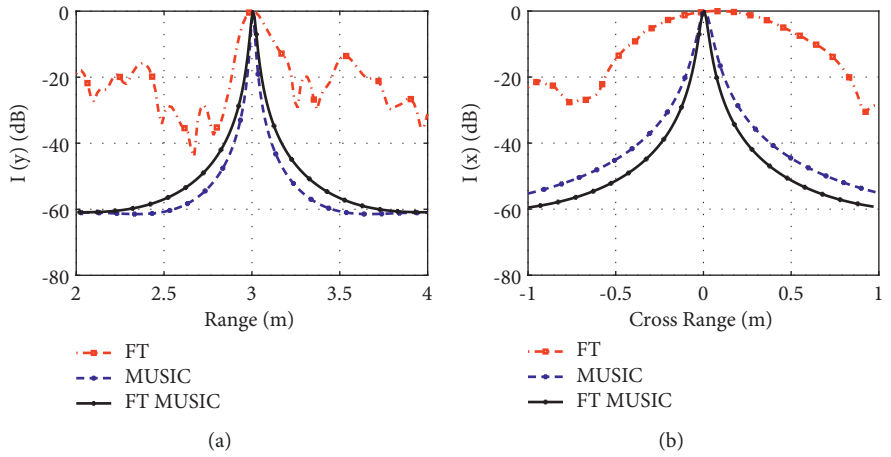

Figure 15: Image cuts along the range (a) and cross-range (b) directions with the MISO radar configuration. A comparison between the three considered techniques is reported in the figure.

Table 1: Comparison among FT, MUSIC, and FT-MUSIC techniques for the MISO and MIMO configurations.

	FT		MUSIC		FT-MUSIC	
	MISO	MIMO	MISO	MIMO	MISO	MIMO
Acquisition time	10 s	20 s	10 s	20 s	10 s	20 s
Elaboration time	1.3 s	1.4 s	3.3 s	3.4 s	1.5 s	1.6 s
Range HPBW for a point target (numerical simulation)	7.0 cm	7.0 cm	1.5 cm	1.5 cm	1.5 cm	1.5 cm
Cross-range HPBW for a point target (numerical simulation)	49.0 cm	31.0 cm	1.5 cm	1.5 cm	1.5 cm	1.5 cm
FOV (3%) for a point target (numerical simulation)	46.2°	47.3°	13.5°	13.5°	45.2°	48.8°
Range HPBW for a metal panel behind a wall (experimental measure)	10 cm	10 cm	3 cm	3 cm	3 cm	3 cm
Cross-range HPBW for a metal panel behind a wall (experimental measure)	60 cm	40 cm	3 cm	3 cm	3 cm	3 cm

From Figure 8(a), it results that the half power beam width (HPBW) for FT is of 7 cm in range both for MIMO and MISO radar configurations, very close to the 7.5 cm predicted by the theoretical resolution. Cross-range HPBW values of 31 cm and 49 cm have been evaluated for the MIMO and MISO radar configuration, respectively [see Figure 8(b)]. These values are very close to the 39 cm and 66 cm predicted by the theoretical resolutions achievable with the MIMO and MISO radar array. Concerning MUSIC and FT-MUSIC, the HPBW in range and cross-range is about 1.5 cm both for MIMO and MISO radar configurations [see Figures 9 and 10].

A further investigation has been performed to evaluate the field of view (FOV) [1] of the two radar configurations and of the three reconstruction techniques. To this end, the point target has been moved in cross-range (dashed black line in Figure 5) at different angles with respect to the antenna center (θ in Figure 5). Figure 11 shows the percentage error on the estimated distance with respect to the real one obtained for the two radar configurations and three considered algorithms. The figure shows that considering a 3% error, the MUSIC algorithm presents a FOV of 15° with overlapping curves for the MIMO and MISO radar configurations. Concerning MUSIC and FT-MUSIC algorithms, the MIMO radar configuration gives rise to results slightly better than the MISO one. However, similar results are achieved with errors lower than 3% up to 45°.

Case 2. Target with clutter

To evaluate the effect of the environmental clutter, two metallic cylindrical targets having radius of 10 cm placed at a cross-distance of 100 cm and located three meters away from the radar antennas were numerically analyzed using the full-wave CST software. In particular, one cylinder models the desired target and the other one an undesired target (clutter). A two-dimensional problem with one waveguide port was considered. The port moves transversely in 16 or 10 positions, at a $\lambda/4$ distance, for the MIMO and MISO cases, respectively. The acquired scattering parameters were processed with the three imaging techniques considered. Since the CST software performs a full-wave analysis, the acquired data take into account the interaction between the two targets. The results of the reconstruction with the three imaging techniques are reported in Figures 12(a) and 12(b) for the MIMO and MISO radars, respectively. The figures show that the FT technique is able to correctly identify the target in the presence of clutter with a separation valley about 20 dB and 10 dB deep for the MIMO and MISO radars, respectively. The presence of the mutual interaction between the targets is evidenced by the small hill between the two peaks. The MUSIC technique presents a behavior similar to the FT one without the central hill. Finally, the FT-MUSIC highlights a deeper valley, but also the presence of an error on the reconstructed distance between the two targets, greater for the MISO radar.

Table 2: Comparison between the proposed radar system and those existing in the literature.

	Type of radar	Frequency range	Average power	Antennas	Algorithms	Max range through wall
Liu and Liu [10]	SISO	0.3–1.3 GHz	10 dBm	1 TX and 1 RX bow-tie	IFT	1.5 m
Mercuri et al. [11]	SISO	7.3–8.3 GHz	0 dBm	1 TX and 1 RX rampart-line	Beam-steering	—
Yan et al. [12]	SISO	0.85–9.55 GHz	1 dBm	1 TX and 1 RX Vivaldi	Variational mode decomposition	2 m
Liu et al. [13]	MISO	0.5–2.5 GHz	3 dBm	1 TX and 8 RX cavity-backed bow-tie	Beamforming	5.5 m
Akiyama et al. [14]	MISO	0.1–1.2 GHz	20 dBm	1 TX and 4 RX spiral	FT	5 m
Salmi and Molisch [15]	MIMO	2–8 GHz	0 dBm	1 TX and 1 RX movable planar monopole	MPC	5 m
Liang et al. [16]	MIMO	0.04–4.4 GHz	10 dBm	2 TX–4 RX spiral	CFAR	5 m
Quinquis et al. [17]	MIMO	11.65–18 GHz	Not available	1 TX and 1 RX movable horn	IFT, MUSIC, ESPRIT	3 m
Yoon and Amin [18]	MIMO	1–3 GHz	10 dBm	2 TX and 1 RX movable horn	Compressive sensing	5 m
Hu et al. [19]	MIMO	0.5–2.5 GHz	1 dBm	8 TX and 8 RX Vivaldi	Back-projection	2 m
This work	MIMO	1–3 GHz	20 dBm	4 TX and 4 RX Vivaldi	FT, MUSIC, FT-MUSIC	≅5 m
	MISO	1–3 GHz	20 dBm	1 TX and 10 RX Vivaldi	FT, MUSIC, FT-MUSIC	≅5 m

FT = Fourier transform, IFT = inverse Fourier transform, MUSIC = multiple signal classification, MPC = multipath components, CFAR=constant false alarm rate, ESPRIT = rotational invariance technique.

Case 3. Panel behind a wall

The experimental scenario investigated consists of a 25-cm-thick tuff wall placed at 2.25 meters from the antenna array and of a 30 cm × 45 cm metal panel placed 50 cm far from the wall (see Figure 13). The wooden support with the antennas was positioned 40 cm above the ground; therefore, the equivalent antenna array central point is located at 66.5 cm from the ground. The MIMO and MISO radar systems previously described have been used to evaluate the scattering parameters at 501 frequency points between 1 and 3 GHz (frequency band $B = 2$ GHz and frequency step $\delta f = 4$ MHz). To reduce the effect of the environment, the scattering parameters used in the reconstruction algorithms were evaluated through the difference between those measured in the presence and absence of the obstacle, thus carrying out a sort of calibration.

To take into account the refraction effect caused by the wall, the hypothesis of an almost normal incidence to the wall by the field generated by the radar has been adopted. In this case, the wall effect can be taken into account by simply adding an additional delay term given by

$$\tau_w = \frac{2\,d}{c}\left(\sqrt{\varepsilon_r'} - 1\right), \tag{19}$$

where d is the wall thickness and ε_r' is the real part of the relative dielectric permittivity. For the relative permittivity of the tuff wall, the value of 3.5 has been used as suggested in [25].

Figures 14 and 15 show the results of the measurements performed using the MIMO (Figure 14) and MISO (Figure 15) radar systems and the three considered reconstruction techniques.

The figures show cuts along the range (a) and cross-range (b) directions of the normalized intensity function performed on the image reconstructions based on the radar configurations and techniques considered. As can be seen, thanks to the τ_w correction, all the techniques correctly reconstruct the distance of the panel. From Figures 14(a) and 15(a), it results that the half power beam width for FT is 10 cm in range both for MIMO and MISO radar configurations. This value is very close to the 7.5 cm theoretical one. Concerning the cross-range HPBW, values of 40 cm and 60 cm have been evaluated for the MIMO and MISO radar configurations, respectively (see Figures 14(b) and 15(b)). These values are slightly higher with respect to those found in the Case 1, and very close to the 39-cm and 66-cm theoretical resolutions achievable with the considered MIMO and MISO arrays. This analysis evidences that both a point scatterer and a 30 cm × 45 cm panel give rise to similar radar images. This confirms the radar theory by which targets with transversal dimensions lower than the cross-range resolution are seen as point scatterers [1].

Concerning MUSIC and FT-MUSIC algorithms, the HPBW in range and cross-range is about 3 cm both for MIMO and MISO radar configurations. This value is twice the one achieved in the Case 1 probably due to the presence of noise and environmental clutter. The achieved values are much smaller than those achieved with the FT algorithm in particular for the cross-range direction. Both the simulated and the experimental study put in evidence the super-resolution properties of the MUSIC algorithm. However, as evidenced in [9] this happens at the expense of a reduced field of view and an increased sensitivity to the environmental noise.

4. Discussion and Conclusions

MIMO and MISO radar techniques based on antenna arrays with approximately the same transverse extension have been compared. In addition, FT, MUSIC, and FT-MUSIC reconstruction techniques applied to two different operative scenarios have been considered. Table 1 summarizes the achieved results. The data reported in the Table 1 show that by using the FT technique, the MISO radar configuration that is realized with 10 antennas has a lower cross-range resolution than the MIMO one, which is made up of 16 equivalent antennas, while the range resolution, being related to the signal bandwidth, is the same for the two configurations.

Concerning MUSIC and FT-MUSIC techniques, both MIMO and MISO radar configurations present similar range and cross-range resolutions. The field of view for FT and FT-MUSIC is about the same, while it is strongly reduced for the MUSIC algorithm. Both MIMO and MISO radars have been realized and used to acquire images of a panel located behind a tuff wall. The HPBWs obtained with the experimental setups are very close to those obtained in the canonical case. As far as the FT technique is concerned, resolutions close to theoretical expectations are obtained. In addition, the super-resolution properties of the MUSIC and FT-MUSIC algorithms are confirmed. These results are not trivial because the experimental data are affected by consistent environmental noise and clutter. Concerning the data acquisition times, the MISO configuration acquires the 501×16 matrix elements in about 20 s, while the MISO radar presents acquisition times of the order of 10 s. Therefore, the use of the MISO radar configuration with a reduced number of antennas determines a reduction of the cross-range resolution of the FT technique but also a reduction in the acquisition time. Finally, it is worth noting that the FT-MUSIC algorithm introduced by the authors presents the same super-resolution properties of the MUSIC one and a field of view comparable with that of the FT technique; therefore, it is a very good candidate for image reconstruction in TWRI systems.

Table 2 reports a comparison between the radar system proposed in this work and those presented in the literature. In particular, the Max Range column refers to measurements reported in the cited articles and does not represent the limit of the aforementioned systems, which is also dependent on the transmitted power and on the type of wall and scatterer considered. As it can be seen, the systems proposed in this work are the most performing among those present in the literature in terms of the number of TX-RX antennas implemented, while they are comparable with the others in terms of maximum range. Furthermore, the possibility to choose between different imaging techniques allows to select the best algorithm according to the scenario to be investigated.

Data Availability

The data that support the findings of this study are available from the corresponding author upon reasonable request.

Conflicts of Interest

The authors declare that they have no conflicts of interest.

References

[1] G. L. Charvat, *Small and Short Range Radar Systems*, CRC Press, Boca Raton, 2014.

[2] M. G. Amin, *Through the wall Radar Imaging*", CRC Press, Boca Raton, 2011.

[3] G. Wang, C. Gu, T. Inoue, and C. Li, "A hybrid FMCW-interferometry radar for indoor precise positioning and versatile life activity monitoring," *IEEE Transactions on Microwave Theory and Techniques*, vol. 62, no. 11, pp. 2812–2822, November. 2014.

[4] G. L. Charvat, L. C. Kempel, E. J. Rothwell, C. M. Coleman, and E. L. Mokole, "A through-dielectric radar imaging system," *IEEE Transactions on Antennas and Propagation*, vol. 58, no. 8, pp. 2594–2603, August. 2010.

[5] G. Sacco, E. Piuzzi, E. Pittella, and S. Pisa, "An FMCW radar for localization and vital signs measurement for different chest orientations," *Sensors*, vol. 20, no. 12, pp. 3489–3514, June 2020.

[6] M. A. Ressler, L. H. Nguyen, F. J. Koenig, and G. Smith, *Synchronous Impulse Reconstruction (SIRE) Radar Sensor for Autonomous Navigation*, US Army Research Laboratory, Adelphi, Maryland, 2006.

[7] S. Pisa, P. Bernardi, M. Cavagnaro, E. Pittella, and E. Piuzzi, "A circuit model of an ultra wideband impulse radar system for breath-activity monitoring," *International Journal of Numerical Modelling: Electronic Networks, Devices and Fields*, vol. 25, no. 1, pp. 46–63, 2012.

[8] X. P. Masbernat, M. G. Amin, F. Ahmad, and C. Ioana, "An MIMO-MTI approach for through-the-wall radar imaging applications," in *Proceedings of the 5th Int. Waveform Diversity and Design Conf*, pp. 188–192, Niagara Falls, ON, Canada, August 2010.

[9] R. Cicchetti, S. Pisa, E. Piuzzi, and E. P. O. Pittella, "Numerical and experimental comparison among a new hybrid FT-Music technique and existing algorithms for through-the-wall radar imaging," *IEEE Transactions on Microwave Theory and Techniques*, vol. 69, no. 7, pp. 3372–3387, July 2021.

[10] L. Liu and S. Liu, "Remote detection of human vital sign with stepped-frequency continuous wave radar," *Ieee Journal of Selected Topics in Applied Earth Observations and Remote Sensing*, vol. 7, no. 3, pp. 775–782, March 2014.

[11] M. Mercuri, G. Sacco, R. Hornung et al., "2-D localization, angular separation and vital signs monitoring using a SISO FMCW Radar for smart long-term health monitoring environments," *IEEE Internet of Things Journal*, vol. 8, no. 14, pp. 11065–11077, July 2021.

[12] J. Yan, H. Hong, H. Zhao, Y. Li, C. Gu, and X. Zhu, "Through-Wall multiple targets vital signs tracking based on VMD algorithm," *Sensors*, vol. 16, no. 8, pp. 1293–1311, August. 2016.

[13] Y. Liu, S. Wu, J. Chen, G. Y. Fang, and H. J. Yin, "Human respiration localization method using UWB linear antenna array," *Journal of Sensors*, vol. 2015, Article ID 601926, 11 pages, 2015.

[14] I. Akiyama, N. Yoshizumi, A. Ohya, Y. Aoki, and F. Matsuno, "Search for survivors buried in rubble by rescue radar with array antennas-extraction of respiratory fluctuation," in *Proceedings of the IEEE International Workshop on Safety,*

Security and Rescue Robotics, no. 1–6, pp. 27–29, Rome, Italy, September. 2007.

[15] J. Salmi and A. F. Molisch, "Propagation parameter estimation, modeling and measurements for ultrawideband MIMO radar," *IEEE Transactions on Antennas and Propagation*, vol. 59, no. 11, pp. 4257–4267, November. 2011.

[16] F. Liang, F. Qi, Q. An et al., "Detection of multiple stationary humans using UWB MIMO radar," *Sensors*, vol. 16, no. 11, pp. 1922–2017, November. 2016.

[17] A. Quinquis, E. Radoi, and F.-C. Totir, "Some radar imagery results using superresolution techniques," *IEEE Transactions on Antennas and Propagation*, vol. 52, no. 5, pp. 1230–1244, May 2004.

[18] Y.-S. Yoon and M. G. Amin, "High-resolution through-the-wall radar imaging using beamspace MUSIC," *IEEE Transactions on Antennas and Propagation*, vol. 56, no. 6, pp. 1763–1774, June. 2008.

[19] Z. Hu, Z. Zeng, K. Wang et al., "Design and analysis of a UWB MIMO radar system with miniaturized Vivaldi antenna for through-wall imaging," *Remote Sensing*, vol. 11, no. 16, p. 1867, 2019.

[20] F. Fioranelli, S. Salous, I. Ndip, and X. Raimundo, "Through-the-wall detection with gated FMCW signals using optimized patch-like and Vivaldi antennas," *IEEE Transactions on Antennas and Propagation*, vol. 63, no. 3, pp. 1106–1117, March. 2015.

[21] S. Pisa, E. Piuzzi, E. Pittella, P. D'Atanasio, A. Zambotti, and G. Sacco, "Comparison between delay and sum and range migration algorithms for image reconstruction in through-the-wall radar imaging systems," *IEEE Journal of Electromagnetics, RF and Microwaves in Medicine and Biology*, vol. 2, no. 4, pp. 270–276, December. 2018.

[22] J. E. Peabody, G. L. Charvat, J. Goodwin, and M. Tobias, "Through-wall imaging radar," *Lincoln Laboratory Journal*, vol. 9, no. 1, pp. 62–72, 2012.

[23] S. Pisa, R. Cicchetti, E. Piuzzi, O. Testa, and P. D'Atanasio, "A multiple input single output radar for through-the-wall radar imaging," in *Proceedings of the 2021 XXXIVth General Assembly and Scientific Symposium of the International Union of Radio Science (URSI GASS)*, pp. 1–4, Rome, Italy, September. 2021.

[24] R. Cicchetti, E. Miozzi, and O. Testa, "Wideband and UWB antennas for wireless applications: a comprehensive review," *International Journal of Antennas and Propagation*, vol. 201745 pages, Article ID 2390808, 2017.

[25] R. Agliata, L. Mollo, and R. Greco, "Use of TDR to compare rising damp in three tuff walls made with different mortars," *Journal of Materials in Civil Engineering*, vol. 29, pp. 1–7, November. 2016.